



HAL
open science

A versatile micromodel technology to explore biofilm development in porous media flows

Christos I. Papadopoulos, Larue Anne Edith, Clara Toulouze, Omar Mokhtari, Julien Lefort, Emmanuel Libert, Pauline Assemat, Pascal Swider, Laurent Malaquin, Yohan Davit

► To cite this version:

Christos I. Papadopoulos, Larue Anne Edith, Clara Toulouze, Omar Mokhtari, Julien Lefort, et al.. A versatile micromodel technology to explore biofilm development in porous media flows. Lab on a Chip, 2024, 24 (2), pp.254-271. 10.1039/D3LC00293D . hal-04798978

HAL Id: hal-04798978

<https://hal.science/hal-04798978v1>

Submitted on 22 Nov 2024

HAL is a multi-disciplinary open access archive for the deposit and dissemination of scientific research documents, whether they are published or not. The documents may come from teaching and research institutions in France or abroad, or from public or private research centers.

L'archive ouverte pluridisciplinaire **HAL**, est destinée au dépôt et à la diffusion de documents scientifiques de niveau recherche, publiés ou non, émanant des établissements d'enseignement et de recherche français ou étrangers, des laboratoires publics ou privés.

A versatile micromodel technology to explore biofilm development in porous media flows

Christos Papadopoulos^{a,b}, Anne Edith Larue^{a,c}, Clara Toulouze^a, Omar Mokhtari^d, Julien Lefort^a, Emmanuel Libert^a, Pauline Assémat^a, Pascal Swider^a, Laurent Malaquin^b and Yohan Davit^{a,*}

Bacterial biofilms that grow in porous media are critical to ecosystem processes and applications ranging from soil bioremediation to bioreactors for treating wastewater or producing value-added products. However, understanding and engineering the complex phenomena that drive the development of biofilms in such systems remains a challenge. Here we present a novel micromodel technology to explore bacterial biofilm development in porous media flows. The technology consists in a set of modules that can be combined as required for any given experiment and conveniently tuned for specific requirements. The core module is a 3D-printed micromodel where biofilm is grown into a perfusable porous substrate. High-precision additive manufacturing, in particular stereolithography, is used to fabricate porous scaffolds with precisely controlled architectures integrating flow channels with diameters down to several hundreds of micrometers. The system is instrumented with: ultraviolet-C light-emitting diodes; on-line measurements of oxygen consumption and pressure drop across the porous medium; camera and spectrophotometric cells for the detection of biofilm detachment events at the outlet. We demonstrate how this technology can be used to study the development of *Pseudomonas aeruginosa* biofilm for several days within a network of flow channels. We find complex dynamics whereby oxygen consumption reaches a steady-state but not the pressure drop, which instead features a permanent regime with large fluctuations. We further use X-ray computed microtomography to image the spatial distribution of biofilms and computational fluid dynamics to link biofilm development with local flow properties. By combining the advantages of additive manufacturing for the creation of reproducible 3D porous microarchitectures with the flow control and instrumentation accuracy of microfluidics, our system provides a platform to study the dynamics of biofilm development in 3D porous media and to rapidly test new concepts in process engineering.

INTRODUCTION

Bacterial biofilms are complex communities that develop on surfaces and interfaces, where the microorganisms are nested in self-secreted extracellular polymeric substances (EPS) **(1)**. This mode of life largely dominates over the free-floating planktonic phenotype **(2)** in a broad variety of environments ranging from the suboceanic subsurface to soils or animal microbiomes. Biofilms are considered an emergent form of bacterial life **(3)** with properties significantly different from that of individual cells. For instance, biofilms are orders of magnitude more resistant to antimicrobials than planktonic bacteria **(4)**. This resilience to treatments imparts a particularly important role to biofilms in medicine, where growth in wounds, on implants, in catheters or in lungs of patients with cystic fibrosis can be life-threatening **(5)**.

In many systems, bacterial biofilms develop in flows on complex substrates. In particular, porous structures provide a suitable and protective environment for biofilm growth, with large surface areas, trapped organic matter and perfusion of nutrients. This is the case in stream sediments and in the hyporheic zone, where biofilms drive ecosystem processes and biogeochemical cycles including carbon and nitrogen **(6)**. Bacterial biofilms can further be used to engineer the properties of porous media **(7,8)**, such as hydraulic conductivity and chemical speciation of soils and materials. Examples include bio-barriers, bioremediation **(9)**, self-healing concrete **(10)**, sealing cap rock fractures in CO₂ storage **(11,12)** or microbially-enhanced oil recovery **(13)** – a tertiary oil extraction technology increasing sweep efficiency via the production of bio-surfactants and selective clogging of pores. In biofilm process engineering of water resources **(14,15)**, the substrate of bioreactors is often some kind of porous medium that increases the amount of biomass per unit volume and facilitates flow. This idea of using flow through porous scaffolds – common in bioreactors for *ex vivo* engineering of living tissues **(16)** – is found, for example, in fixed or fluidized bed reactors **(17)** used in wastewater treatment for the removal of organic matter, nitrates, phosphorus or micro-pollutants. Similar technologies based upon trickling filters, submerged bed, membrane-based and fluidized-bed reactor technologies are also used to produce

^a. Institut de Mécanique des Fluides (IMFT), CNRS & Université de Toulouse, 31400 Toulouse, France.

^b. LAAS-CNRS, CNRS & Université de Toulouse, 31400 Toulouse, France.

^c. Transverse Lab, 271 rue des Fontaines, 31300 Toulouse, France.

^d. Physikalisches Institut, Universität Bern, Gesellschaftsstrasse 6, 3012 Bern.

* Corresponding author (yohan.davit@imft.fr).

value-added products such as fuel ethanol (18) or organic acids (19).

Biofilms growing in porous media flows is a particularly complex process (20) that is not well understood even with single strain biofilms – let alone in biofilms involving a variety of microorganisms. The development of biofilms in porous media is mediated by a range of physical phenomena and biological processes including interactions with the solid surface (21,22), flow (23), oxygen and nutrient transport (24) or quorum sensing (QS) (25). The porous structure tends to create heterogeneities and gradients – velocity, nutrients concentrations, molecular signals, biocides – that strongly affect the behavior of bacteria. For example, at the individual cell level, motility and adhesion in a confined geometry is particularly affected by the large shear rates close to interfaces (26). Low-flow regions, such as dead-end pores, further modulate the persistence of bacteria in different zones of the porous structure (27). At the population level, biological processes such as QS are not uniform spatially but rather depend on the geometry of the substrate and on the flow (28). To add to the complexity, the growth of biofilm also generates clogging, which in turn modifies the flow through the porous structure, and thus mass transport, potentially leading to intermittency (29) and anomalous transport (30). Biofilm streamers can also cause abrupt changes in the flow patterns in porous media through sudden bridging and clogging of pores (31).

Microfluidic approaches have been instrumental in studying the fundamentals of bacterial ecology in flow, complex structures and heterogeneous conditions. Their main advantage is that they provide a high level of control over microenvironments that can be varied in space and time to mimic a variety of conditions (32–34). They can also be combined with molecular biology and optical microscopy to visualize processes from the cellular to the biofilm scale (35). In biofilm engineering, microfluidic reactors further offer a relatively cheap and reproducible way of parallelizing, testing new concepts and optimizing processes, before scaling up for applications (36,37). These reactors have been used to assess the efficacy of newly constructed organisms (38), to develop portable biomanufacturing platforms (39), to screen microbial strains for fermentation processes (40,41) and to test antibiotic susceptibility and toxicity (42).

However, standard manufacturing approaches to fabricate microfluidic chips rely on planar technologies (e.g. soft lithography, micro-milling), which are not adapted to exploring biofilm development in 3D porous media. The geometry and topology of a structure constrained into a plane is very different from that of a 3D porous medium, which leads to fundamental changes in flow and transport properties (43–46). For example, comparisons of simulations in 2D and 3D show that pore connectivity affects couplings between flow and bioclogging, with 2D geometries overestimating fouling-induced changes in the velocity field (47). Further, simple flows at low Reynolds number in PDMS chips only generate a narrow range of shear and pressure stresses that is not representative of the heterogeneity found in many porous media. Since mechanical stresses shape the morphology of biofilms through detachment

(48), the ability to reproduce this heterogeneity in model systems would be an important step forward. Low Reynolds number flows in PDMS chips are also associated with weak mixing of solutes (49–51), whereas flows in 3D porous structures induce strong (chaotic) mixing even at zero Reynolds number (52–54). As many biofilm processes are driven by flow and transport of chemical species, how these molecules are transported through the porous medium and whether they are accessible to bacteria is likely to control many aspects of the ecology of biofilms.

Here, we present a novel porous micromodel technology for bacterial biofilms under flow, which can be used to explore a broader range of three-dimensional geometries and topologies of pore networks. Our approach relies on a “lego-like” design and a range of 3D printed modules (Section **Experimental Setup**) that can be conveniently assembled as needed for a specific experiment. The central module is a micromodel containing a porous medium for biofilm growth. High resolution 3D printing allows us to create arbitrary porous media with controlled architectures including flow channels with a diameter down to several hundreds of micrometers. The micromodel is instrumented to measure the differential pressure across the porous medium, oxygen consumption, optical density at the effluent stream and images of biofilm detachment through monitoring of the effluent using a camera. We show (Section **Results and Discussion**) how this system can be used to study the dynamics of growth and detachment of a biofilm of *Pseudomonas aeruginosa* – the top model microorganism for single-species biofilms. We also demonstrate that it can be advantageously combined with computational fluid dynamics (CFD) and X-ray micro-tomography (μ CT) to link the spatial distribution of the biofilm within the reactor with flow properties.

EXPERIMENTAL SETUP

The proposed experimental setup is designed to be used as a platform to study biofilm growth dynamics in porous media and to test new concepts or organisms in biofilm process engineering. Since the system is to be used for research purposes, we designed it to be versatile and conveniently adaptable to specific experiments. Firstly, we used 3D printing to be able to rapidly modify the different parts according to the needs, to deal with a large range of complex designs, to efficiently prototype, to have good reproducibility and to fabricate dozens of components at once. Reproducibility proved to be of great importance since the system is designed for biological research applications, where (clean/identical) initial conditions are primordial. Secondly, to ensure flexibility in the experimental setup, slip connectors were used for parts that required frequent plugging and unplugging, whereas threaded connectors were preferred for components that needed a stable and leakproof connection throughout the experiment. In both cases, we implemented luer-like connectors – standardized/universal connectors that are widely used for biomedical applications. In the case of slip connectors, the luer-like connectors were equipped with slits to accommodate chemically inert rubber o-rings. These o-rings are an easy-to-

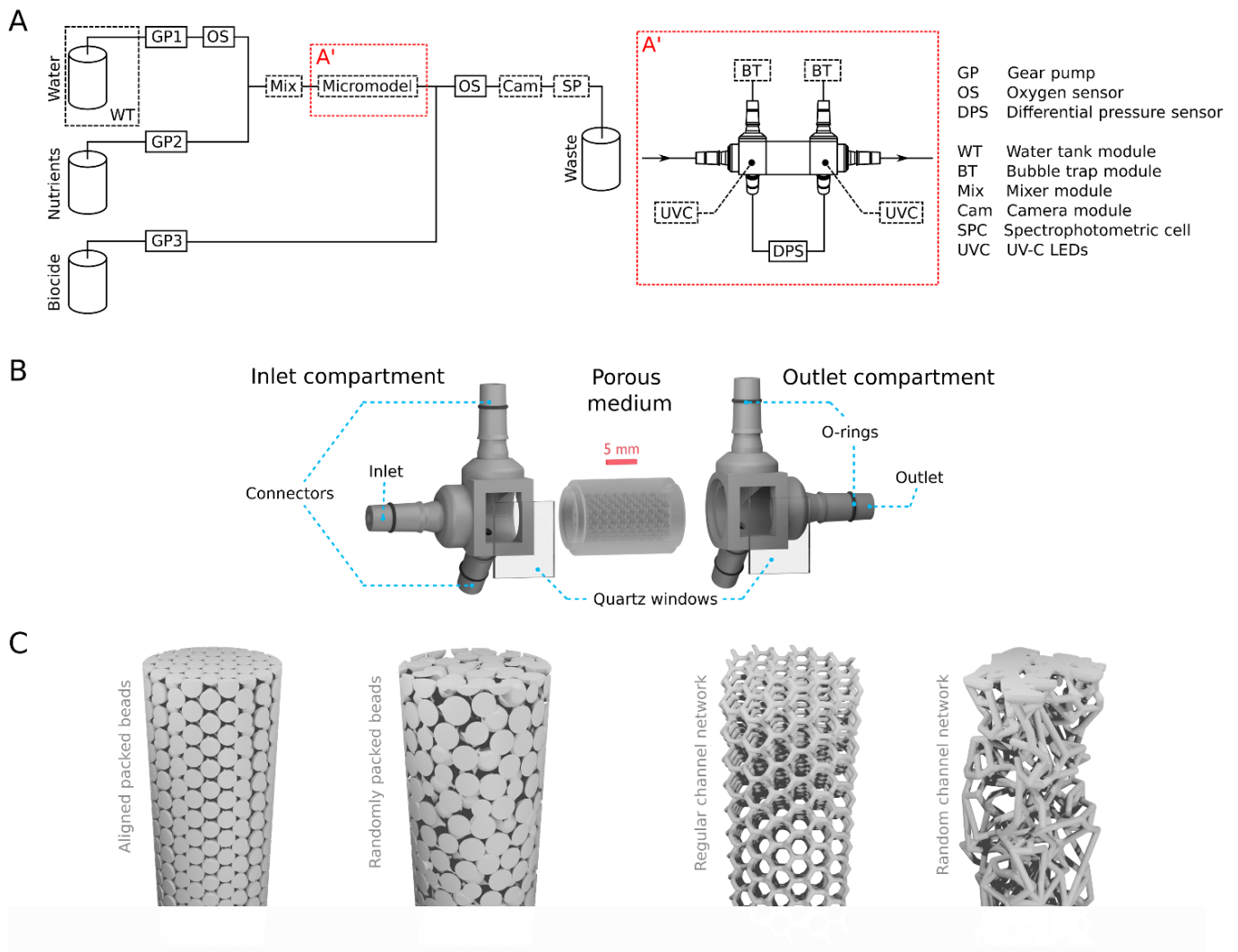


Figure 1 Experimental setup and porous micromodel. (A) Schematic of an example configuration of the experimental setup used to perform biofilm growth dynamics experiments. Inset A' shows a detailed representation of the micromodel. (B) Schematic of the bioreactor in three distinct parts, indicating the different elements integrated. (C) 3D representations of the different porous media printed – images are generated from the initial .stl files. From left to right: aligned packed beads, randomly stacked beads, periodic channel network and random channel network. The beads are 1 mm in diameter while the channels are 300 μm in diameter. Note that the 3D representations of the bead packings correspond to the solid material, while the channels correspond to the empty pore space within the porous medium to better visualize the porous structure.

implement and cheap way to ensure adequate sealing of the connections even after multiple attachments and detachments. The use of both slip and threaded connectors in the experimental setup provided a versatile and adaptable solution that met the various needs of the system.

In the core of the experimental setup lies the micromodel. The main functionality of this micromodel is that it hosts the porous medium used as a substrate for the bacterial biofilm to grow. Around the micromodel, throughout the fluidic circuit, various modules ensure the smooth proceeding of the experiment (fluidic modules and devices) or accommodate the various measurements (instrumentation modules and devices). An example setup is presented in fig. 1A and the different modules are discussed in detail in the remainder of this section.

Micromodel module

The micromodel consists of three parts (fig. 1B). The central part hosts the porous substrate where biofilm growth takes place. The inlet and the outlet compartments are modifiable and are designed for connection to the various fluidic modules and measuring devices. Examples of such modules include water/nutrient and detergent injection inlets, bubble traps, connectors to differential pressure sensors and oxygen sensors (see fig. 1A). Each part is printed using a different 3D printing technique, adapted to the needs of each component.

The porous medium The central part of the micromodel is the porous medium (fig. 1B). Figure 1C shows example porous structures that were fabricated: aligned and randomly stacked beads, regular and irregular channel. For fabrication, both stereolithography (SLA) and multi jet printing (MJP) were implemented. The SLA technique (resolution down to 30 μm

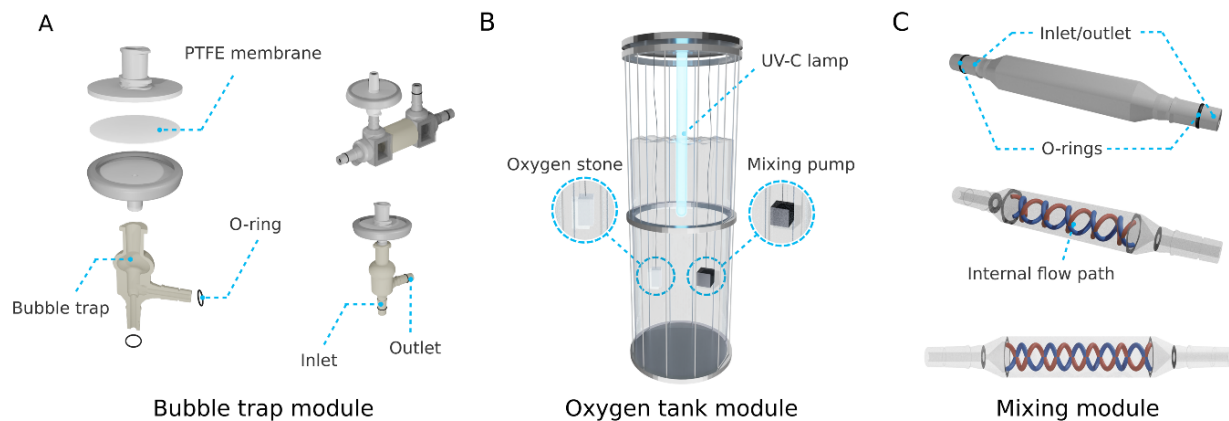


Figure 2 Fluid modules. (A) (Left and right bottom) Bubble trap module. The bottom, 3D-printed part naturally directs incoming bubbles towards the PTFE membrane filter where the bubble is evacuated. (Right top) The PTFE membrane can also be directly mounted onto the bioreactor inlet and outlet compartment modules. (B) The water tank module is equipped with a UVC bactericidal lamp, an oxygenating stone and a mixing pump to ensure homogeneity of oxygen concentration. (C) The mixer module is a 3D-printed part that is designed with a double helicoidal coil to ensure the proper mixing of streams.

(X,Y) and 10 μm in Z direction) was found to be optimal for 3D-printing channel networks with channel diameters down to 300 μm , while it was possible to 3D-print bead-like structures only by using the MJF technique (resolution down to 32 μm in Z direction) due to the fact that in certain regions, beads are freely hanging in space and therefore a support material is needed.

Inlet and outlet compartments The two compartments of the micromodel (Fig. 1B), attached on the two ends of the porous medium, are designed to accommodate mainly the fluid inlets and outlets, but also serve to attach various fluidic and instrumentation modules. Nutrients and oxygenated water come in at the inlet compartment, flow through the porous medium and are then directed out of the micromodel from the outlet compartment. Both inlet and outlet compartments have connectors for the pressure sensor that measures the differential pressure induced by the imposed inlet flowrate within the porous medium. Both compartments are equipped with one rectangular opening in each side, covered with a quartz window. This design allows for the continuous illumination of both compartments with bactericidal ultraviolet-C (UVC) light and therefore for the confinement of bacterial development within the limits of the porous medium.

Fluid module 1: Bubble traps

Air bubble formation is a common phenomenon throughout such fluidic systems, especially when the fluid stream is at the dissolved oxygen saturation levels when injected into the system. These bubbles can disrupt the various measurements but also promote biofilm detachment when they flow through the porous medium(55). The bubble trap module can be used wherever needed throughout the fluidic circuit. A central element of this module is the hydrophobic PTFE membrane filter with 0.45 μm pore size. When the filter is placed upwards, passing bubbles are naturally flowing towards the membrane and due to its hydrophobic nature, the bubbles are evacuated

from the fluidic circuit without leakage. The filter membrane can be directly fixed onto the micromodel, at one of its inlets/outlets, but it can also be placed wherever it is needed throughout the microfluidic circuit by adding a secondary element to the module. This element is a 3D-printed part that is designed with one vertical fluidic inlet on the bottom, one horizontal fluidic outlet, an outlet on the top where the membrane filter is fixed and a compartment in the middle to amplify the trapping effect of the bubble trap module (see fig. 2A).

Fluid module 2: Water tank

A specific water tank module (fig. 2B) was designed as the main water supply. Sterility of the streams is important especially when a specific strain is studied. For this, the tank is equipped with a bactericidal UVC lamp which continuously irradiates UVC light throughout the duration of an experiment. Each water tank consists of a 70 cm transparent Lexan tube of internal diameter of 20 cm which translates to roughly 20 liters of stored water. This allows for an experiment at 2 ml/min to run for more than three days without the need for a refill. In addition, the module accommodates a ceramic stone that facilitates the supply of a gas to be dissolved in the water such as pressurized air, nitrogen, or pure oxygen. Finally, a mixing pump ensures homogeneity of gas concentrations throughout the bulk of the liquid.

Fluid module 3: Mixer

In the low-Reynolds number regime that dominates micro-devices, mixing can be challenging and lead to unwanted heterogeneities. A 3D-printed fluidic module (fig. 2C) was implemented to ensure proper mixing of two streams wherever needed throughout the experimental setup, for example to mix concentrated nutrients with water (fig. 1A) or to mix a colored dye with water for breakthrough curves. The mixer consists of two helicoidal channels of 1mm in diameter each, one spinning

clockwise and one anti-clockwise, with multiple meeting points forcing the fluid flowing through to mix.

Instrumentation module 1: Spectrophotometric cell

Spectrophotometric measurements of fluid streams provide information about the contents of the stream for example to measure the optical density of a stream loaded with biomass, perform tracing tests with colored dyes through the system to study the hydrodynamic properties such as retention times and breakthrough curves, or use it to detect solid/semi-solid objects passing through the stream. This module consists of two spectrophotometers, two homemade 3D-printed flow cells and a light source with two light probes. Each flow cell is fabricated using four parts and a quartz window. The cell is designed to have a light path of 1.2 mm. For each cell, the optic fiber of the spectrophotometer is fixed on the one side of the cell, while the tip of the light source probe is placed on the other side (fig. 3A). One cell is connected to the fluidic circuit to be measured for its optical density (OD) while the other one is directly measuring the light intensity of the source without being connected to the fluidic circuit. Like so, the signal obtained from the reference cell is used as a baseline for the calculation of the absorption, eliminating any erroneous signal due to source light intensity fluctuations.

Instrumentation module 2: Camera cell

Biofilm development under flow is a dynamic process with a strong competition between growth and detachment. We therefore designed a cell that can be used to image biofilm patches that detach from within the porous medium and analyze the dynamics of this detachment. This module is meant to be installed at the effluent stream, after the detergent injection to ensure that there is no biofilm colonization on the cell that would disrupt the measurements. The whole module (fig. 3B) consists of a 3D-printed flow cell, a camera and a light source. As biofilm patches flow through the flow cell (3D-printed with two quartz windows), they are captured by the camera through a dark field imaging approach.

As shown in fig. 1A, biofilm detachment events can be studied using both camera and spectrophotometric cells. These modules offer complementary information to one another. The spectrophotometric cell can detect detached biofilm patches continuously throughout long experiments lasting several days. Meanwhile, the camera cell module generates a significant amount of data and requires extensive post-processing of videos, which can be time-consuming and computationally intensive. However, it provides additional information about the size of the biofilm patches that pass through the effluent stream.

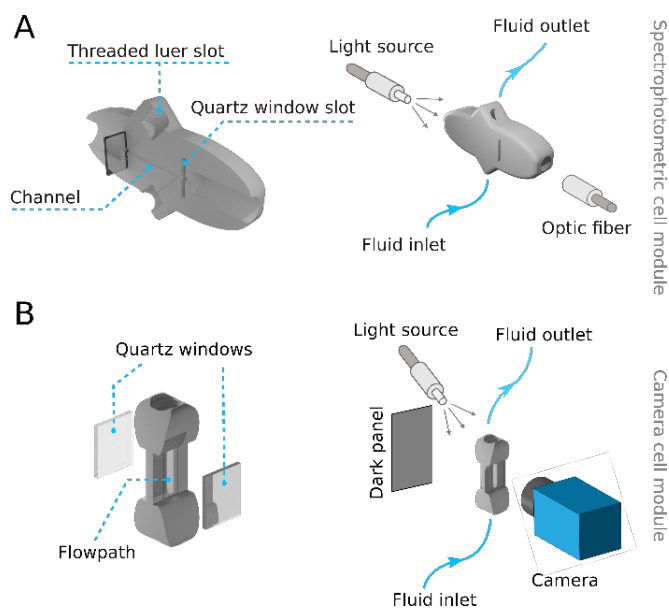


Figure 3 Instrumentation modules. (A) Schematics of the spectrophotometric cell, which consists of several 3D-printed parts and a quartz glass. The light source probe is fixed on the one side of the module, so the light is directed through the 1.2 mm in diameter fluidic channel and the quartz window, towards the side of the module where the sensor is located. (B) The camera module consists of two quartz windows and a 3D-printed channel of 2 mm width and 10 mm of length. To perform darkfield imaging, the light source is placed behind the camera cell with a certain angle so that it does not directly illuminate the cell while the camera is placed directly adjacent on the other side of the cell. Directly opposite of the camera, a dark panel prevents stray light from reaching the camera.

MATERIALS AND METHODS

Microfabrication using SLA Stereolithography (SLA) microfabrication was performed using a DWS 29J+ (DWS Systems) printer. The resin used (DS3000) is a semi-transparent biocompatible acrylic resin (DWS Systems). The 3D printing method, combined with this resin, offers a relatively high resolution of 30 μm in the X and Y direction and an adjustable layer thickness in the Z direction (between 10 to 100 μm). The pieces were post-treated with ethanol and isopropanol to evacuate the unpolymerized resin from within the crevices and they were further cured with UV light at 405 nm for 30 minutes to ensure the full polymerization of the resin and minimize cytotoxicity. Structures were printed using the following parameters for the main body of the 3D pieces: indentation 0.01, hatching 0.04, Z-compensation 0.12, laser speed 5800 and contour 0. The parameter “contour” controls the extra layers of material that are added to the surface of the 3D printed structure. Increasing the number of layers, provides a smoother surface but tends to produce oversized structures and wider crevices. Keeping contour to 0, slightly undervalues the size of material-filled structures.

Fabrication using MJP For the fabrication of 3D pieces using the MJP technique, we used a ProJet MJP 2500 plus (3D Systems) with the resin VisiJet M2R-TN as the main printing material and VisiJet M2 SUP as the support wax material. The printing resolution is about 32 μm per layer. After being printed, all the

pieces were placed in the oven at 70°C for at least one day or until all of the support material was removed.

Design of porous structures (CAD) The aligned and the random bead packing structures were designed using the open-source software Blender (56). In both cases, the beads were designed to be 1mm in diameter. The random bead packing was generated by simulating falling 1mm-diameter beads in a beaker using Blender. The random channel network, with channels of varying orientation and length, was created from a homemade code (57), designed for control of various parameters, such as node connectivity and density, range of channel length, minimum angle between channels, and removal of border dead-end channels. Originally used for brain vascular networks, this code was modified for the current study to generate a channel network with a target channel diameter of 200 µm, a connectivity of 3 for each node. The code produced a binary tiff image stack that was thresholded using Avizo to reproduce the 3D volume. The periodic network was modelled after a Laves graph (58) with a target channel diameter of 300µm, each edge of length 700µm, a connectivity of 3 for each node. It was designed as a spatial graph comprising of vertices and edges and then transformed into a binarized tiff stack using a homemade Python code. A 3D surface was finally extracted from the tiff stack using Avizo software.

Assembly of 3D-printed modules The three parts of the micromodel were assembled together using an instant, cyanoacrylate glue (Colle Fix, Würth France), while the UVC windows are fixed in place with a UV cured glue (NOA81, Norland). All the parts of the spectrophotometric as well as the windows of the camera cell were glued in place with the same UV cured glue. After being assembled, the spectrophotometric cell was painted with a black mat spray paint in order to eliminate external light perturbations.

Bacterial culture The bacterial strain used is *Pseudomonas aeruginosa* (ATCC 15692 GFP). *Pseudomonas aeruginosa* was selected because of its ability to form single-species biofilm, making it the most common model organism for biofilm studies. More specifically, the ATCC 15692 GFP strain was selected because: 1) it makes it possible to complement 3D micromodel experiments with fluorescence microscopy in PDMS microfluidics and 2) the plasmid provides ampicillin resistance that helps avoid contaminations. The strain is taken out of a -80°C stock and is incubated overnight in 20 mL of Brain Heart Infusion broth at 37.5 mg/mL (BHI, Merck) with 300 µg/mL ampicillin (ThermoFisher Scientific) at 30°C and 180 RPM. The next day, the solution is diluted until an optical density of 0.5 at 600 nm (OD₆₀₀) is obtained. This ensures consistent initial conditions of biofilm growth. The inoculation procedure of the micromodel starts with ethanol injection (about 10 mL) to ensure a sterile environment while ejecting air bubbles from within the porous medium. Next, about 10 mL of sterilized BHI solution (37.5 mg/mL) with ampicillin (300 µg/mL) is used to displace the ethanol and finally, 10 mL of the inoculum is injected. After inoculation, the inlet and outlet of the micromodel are sealed and the micromodel is placed in the incubator at 37°C for one hour.

Sterilization of the system and solution preparation To reduce external contaminations throughout the whole system and fouling by *Pseudomonas aeruginosa* outside the porous medium, several strategies were implemented. All of the tubing and the luer-like connectors were autoclaved prior to the experiments (121°C, 15 min). The detergent solution (Tergazyme 5.5% g/L, Alconox), that was injected directly at the outlet compartment, neutralizes planktonic bacteria and reduces attachment of biofilm patches flowing out of the porous medium. Tergazyme is an enzyme-active detergent that contains a mixture of anionic surfactants and protease enzyme. A UVC lamp was used to illuminate the water tank from which water was supplied to the system. A second UVC lamp placed in front of the quartz windows located at the inlet and outlet compartments of the micromodel, ensured that biofilm growth is taking place only in the porous medium and reducing the risk of a contamination by other bacteria. Finally, the nutrient solution (BHI, 37.5% w/w) contained 300 µg/mL of ampicillin, an antibiotic to which the bacterial strain used in this experiment is resistant.

Connecting modules All 3D-printed fluidic connections of the micromodel were designed as luer-like connectors, a standardized design that is compatible with many commercial fluidic connectors. Additionally, these connectors were designed to facilitate nitrile rubber o-rings (3.2 mm ID, 4.2 mm OD) to ensure leakproofness while maintaining ease of use. The camera and the spectrophotometric cells were designed with threaded luer-like fittings to directly connect them to the tubing since no unplugging was needed at any point during the experiment. The tubing used for all the experiments was Novosil silicon flexible tubing (0.75mm ID, 1.5mm OD) apart from the one used with the differential pressure sensors (PTFE internal diameter 0.56mm, external diameter 1.07mm). Prior to each experiment, the tubings attached to each side of the pressure sensor were filled with water and sealed until the start of the experiment, when they were attached on the two bottom inlets of the micromodel.

Flow regulation To supply the different streams, two different types of gear pumps were used, each with an adapted flowrate range according to the needs of the supplied stream. The water stream was supplied at a flowrate of 1.8 mL/min using a gear pump (mzr-2921x1, HNP Mikrosysteme). For the nutrients and the detergent stream, the two pumps (mzr-2521x1, HNP Mikrosysteme) provided a flowrate of 0.2 mL/min each. For the flowrates chosen, the precision is about 1 % CV (coefficient of variation). These pumps can work within a differential pressure range of 0-3 bars for the mzr-2921x1 and 0-1.5 bars for the mzr-2521x1, liquid temperature range of -20 to 60 °C and viscosity range of 0.3 - 100 mPa·s. The gear pumps were calibrated prior to each experiment by recalculating a calibration factor. This was done by fixing the flowrate at the desired value and measuring the dispensed volume of water for a given period.

Oxygenation of the water tanks For the biofilm growth experiments, oxygenated water was supplied to ensure the required oxygen levels. The water tanks were bubbled with oxygen until reaching about 8.5 mg/L of dissolved oxygen at 25°C. To achieve this, a mixture of pressurized air and oxygen

was bubbled through a ceramic stone placed within the tank. The process of oxygenating the water tanks commenced at least one hour prior to the start of each experiment. Once saturation levels were achieved, the bubbling process was halted. To ensure uniform oxygen distribution throughout the liquid, a small aquarium pump was utilized to maintain continuous stirring of the ultra-pure water.

Oxygen measurements The oxygen sensors (FTCH-PSt1, Presens GmbH), connected to the control unit (OXY-4 micro, Presens), were cleaned prior to each experiment by letting them sit in an 1% Tergazyme solution for at least 30 mins to remove residual organic matter. For the data acquisition, the oxygen sensors were calibrated according to the procedure described below and a 15 minutes measuring interval was selected. The temperature had to be manually imported to the software so the mean room temperature was selected at 25°C. The volume inside the measuring cell was about 310 µL, the O₂ measurement range was from 0 to 22.5 mg/L of dissolved O₂. The resolution of the measurements depends on the oxygen concentration. For the oxygen levels measured in this work, the resolution of the probes is about ± 0.04 mg/L. The sensor's tip is located within the measuring cell. This tip has a diameter of less than 50 µm, on the edge of which there is a membrane with a luminophore. The operating principle is based on the effect of dynamic luminescence quenching by molecular oxygen. The light emitted by the source (633 nm) is directed through the sensor's tip towards the luminophore present at the edge of the tip and briefly excites the luminophore, which in turn emits light. In presence of oxygen, the luminophore is quenched. The intensity of light received by the sensor is therefore translated into oxygen concentration.

Calibration of oxygen sensors Prior to starting the experiments, the oxygen sensors were calibrated by performing a two-point calibration. A 100% saturated oxygen solution was prepared by bubbling pressurized air into a bottle filled with 100 ml of DI water for 15 minutes and then the solution was left with an open lid under magnetic stirring to ensure that there is no oversaturation in oxygen. An oxygen-free water solution was prepared by dissolving 1 g of sodium sulfite (Na₂SO₃) and 50 µL of cobalt nitrate solution (500 mM Co(NO₃)₂) in 100 mL of water. The bottle was closed and shaken for several minutes to dissolve the sodium sulfite and ensure the water is oxygen-free.

Quartz windows The quartz slides used to fabricate the rectangular windows (42297 Quartz microscope slide, fused, Alfa Aesar) used for the bioreactor, the spectrophotometric and the camera cells were cut using a diamond saw to the required dimensions (12x10x1 mm). The rectangles were washed in pure isopropanol and put in a sonication bath for 10 minutes to ensure cleanliness. Then, the rectangular slides were dried using compressed air in order not to introduce dust and other particles and were fixed in place using a fast-curing optical adhesive (NOA81, Norland). The gluing region was consequently exposed to UVC light with a wavelength centered at 365 nm.

Electrical engineering for UVC LEDs and UVC lamps To illuminate the water tanks, a bactericidal UVC lamp (UV-technik GmbH) was

used, working at 16 W. To illuminate the micromodel's inlet and outlet compartment, a couple of UVC LEDs (Klaran, 70 mW KL265-50V-SM-WD) irradiating at 265 nm were used. The two LEDs were placed one centimeter away, in front of the micromodel windows throughout the biofilm growth experiments. The intensity of the UVC LEDs was regulated by a homemade electronic controller connected to a computer. *In situ* measurements of the irradiance were performed using a photo/radiometer (Delta Ohm Portable Luxmeter HD 2102.1) connected to a UVC probe (Delta Ohm LP471UVC). The measurement was performed at 1 cm distance between the source and the sensor with a quartz window of 1 mm thickness in between and the effective irradiance passing through was found to be 13.6 W/m² (1.36 mW/cm²). Eliminating completely parasitic growth is difficult, as biofilm formation tends to shield microorganisms from UVC (59). However, such irradiance has been found to considerably limit contamination and parasitic growth of *P. aeruginosa* biofilm (60). In ideal conditions, the attenuation coefficient of the liquid passing through the bioreactor should be in the range of 1 cm⁻¹, or lower, to ensure that the irradiation is sufficient throughout the system. If the absorption coefficient is larger, the design of the bioreactor can be modified to implement two quartz slides – one on each side – to reduce the travel distance of UVC to reach the microorganisms.

Differential pressure measurements The differential pressure sensors (Keller Series PD-33X) have a single silicon diaphragm in their interior, which is pressurized from both sides and measures the pressure difference directly. The transmitters use digital compensation with a mathematical model to achieve accuracy of 0.05% FS (percentage of full scale) – in the temperature range from 10 to 40 °C. The device is also measuring the ambient temperature. The pressure sensors were cleaned with a cleaning agent (Decon90, Decon) and disinfected with 70% v/v ethanol before and after each experiment.

Determination of biofilm growth phase through model fitting The differential pressure data obtained during the biofilm growth experiments were fitted to the following logistic function (eq. 1)

$$f(t) = \frac{\overline{\Delta P}}{1 + e^{-\frac{(t-t_1)}{\tau}}} \quad (1)$$

where $\overline{\Delta P}$ is the supremum of the values of the function, t_1 the value of the function's midpoint and τ the logistic growth characteristic time of the curve. In addition, we define t_0 as the timepoint where the curve is at 5% of its maximum value. t_0 is used to characterize the transition from phase I to phase II of biofilm growth (detailed in results section). In addition, t_2 is the time point where the function is at 95% of its maximum value and it denotes the beginning of phase III of biofilm growth. The differential pressure data from seven (n=7) biofilm growth experiments using the same growth conditions were analyzed and their fitted parameters were compared. We also defined $\sigma(\overline{\Delta P})$ as the mean standard deviation of fluctuations about $\overline{\Delta P}$ for those experiments.

Determination of the initial permeability of porous media The initial permeability of the porous medium was determined by measuring the differential pressure at several flowrates using a gear pump. The experiment was carried out by first setting the flowrate to zero and zeroing the measuring device of the differential pressure as part of calibration. Then, several different flowrates were imposed, and the corresponding differential pressures were recorded. A linear fit was performed on the data to extract the initial permeability of the system using Darcy's law of permeability (see supplementary information fig. S1)

$$q = \frac{kS}{\mu L} \Delta P \quad (2)$$

where q is the imposed flowrate, μ is the dynamic viscosity of the fluid (here we make the assumption that it is the same as that of water at 25°C, 0.8891 mPa·s), k the permeability of the medium, S is the cross-section area of the porous medium (12.566 mm²) and Δp the pressure drop over the distance between the inlet and the outlet of the porous medium L (14 mm).

Spectrophotometric module data acquisition For these measurements, two OceanOptics spectrophotometers (OceanOptics USB2000+) and a ZEISS light source (Zeiss CL 9000 LED) with two outlets were used. One spectrophotometer was directly attached onto one light source outlet so that it measures the light intensity fluctuations of the source which would be used as a reference. The second spectrophotometer's optical fiber was mounted on the homemade 3D-printed spectrophotometric cell with the other outlet of the light source on the other side of the cell, as shown in Figure 3. For the acquisition, the light intensity of the source was fixed so that the received light does not oversaturate any of the two spectrophotometers. The light intensity was recorded at approximately 0.1 s interval with no averaging of the values, with a boxcar width of 10, at 600 nm wavelength. The absorption was deduced from the light intensity data according to

$$A(t) = \log_{10} \left(\underbrace{\frac{I(t) - I_{\text{dark}}}{I(t=0) - I_{\text{dark}}}}_{\text{Standard expression}} \times \underbrace{\frac{I^{\text{ref}}(t=0) - I_{\text{dark}}^{\text{ref}}}{I^{\text{ref}}(t) - I_{\text{dark}}^{\text{ref}}}}_{\text{Fluctuation correction}} \right) \quad (3)$$

where $A(t)$ is the calculated absorption, I_{dark} and $I_{\text{dark}}^{\text{ref}}$ are respectively the light intensity signals of the main and the reference spectrophotometers in the absence of light, $I(t=0)$ and $I^{\text{ref}}(t=0)$ are respectively the initial light intensity received by the main and the reference spectrophotometers, $I(t)$ and $I^{\text{ref}}(t)$ are respectively the light intensity data of the two spectrophotometers. t is the time with (t) indicating the variables that are functions of time.

Data acquisition with camera cell Initially the camera (PCO edge) is placed in front of the camera cell and the light source (Olympus KL 2500 LED) angle is adjusted so that the camera is not overexposed while receiving adequate light at a fixed exposure time (65 ms). The diaphragm of the lenses was placed at its closed position. The camera has 2000x400 pixels. A binning of 2x2 was selected to increase the signal of each pixel while reducing the unnecessarily high number of pixels, and therefore the data size, by a factor of 4. The final image was approximately 8.2 $\mu\text{m}/\text{pixels}$ after binning. The framerate acquisition was high enough to capture phenomena such as biofilm detachment events.

Camera module video processing Videos obtained from the camera were exported as tiff image stacks and were processed using a homemade MATLAB R2022b script. The image sequences were rotated, and the area of interest was cropped in order to keep only the main flow channel of the cell. The image stacks were then thresholded and the mean pixel value of each frame was measured. A baseline of the signal was calculated using the moving average method considering 100 neighboring datapoints. The baseline was subtracted from the signal in order to remove trends related to persistent biofilm patches that were attached in the camera cell. The findpeaks function in MATLAB was implemented to locate signal peaks with minimum peak prominence set to 0.02 and minimum peak height to 0.005. Finally, the known size of the channel width was used to correlate the pixel number to biofilm patch area in each frame (0.826 $\mu\text{m}^2/\text{pixel}$).

Cross-correlation analysis of camera and spectrophotometric cell data Cross-correlation analysis was performed between the data obtained from the spectrophotometric measurements and the camera cell from time 68 h to time 86 h. This range was selected since it is within the last phase (permanent regime) of biofilm growth and therefore we expect both signals to behave in a similar way, with peaks appearing whenever a biofilm patch goes through each respective module. Prior to performing cross-correlation analysis, both datasets were resampled at 20 Hz to ensure homogeneous distribution of the data.

Fourier analysis of camera and spectrophotometric data The spectrophotometric and the camera data were analyzed using the fast Fourier transform algorithm for discrete Fourier transform analysis (DFT) in MATLAB. Data from 68 to 86 hours were selected to be analyzed as that was the available time range in the case of the camera module. The data in both cases were resampled to make sure that they are equally spaced and have a constant sampling rate along the sampling period. In the case of spectrophotometric data, the sampling period is 0.1 s (sampling frequency 10 s⁻¹) and in the case of camera data, the sampling period is 0.065 s (sampling frequency 15.38 s⁻¹).

X-ray computed microtomography All of the X-ray imaging of the various porous structures, as well as that of the biofilm inoculated porous medium, was performed with the same scanning parameters. The X-ray tomograph (EasyTom XL 150, RX Solutions) was equipped with a sealed-tube X-ray source (Micro 150, RX Solutions) capable of delivering 75W maximum power and a flat panel sensor with a pixel matrix of 1920x1536 pixels. Imaging was performed at 60 kV tube

voltage and 165 μA tube current with a frame rate of 2 images per second and averaging 8 images per projection. By adjusting the position of the sample relative to the source and the sensor, a voxel size of 9 μm was achieved.

Contrast agents for biofilm imaging The staining procedure is adapted from (61,62). The idea of the approach is to inject a suspension of barium sulfate inside the porous medium, with particles that are sufficiently large so as not to penetrate inside the biofilm. This increases the X-ray absorption of the pore space except for the volume fraction with biofilm and thus provides a form of negative contrast. The suspension of barium sulfate is further mixed with a gelling agent in order to limit sedimentation during acquisition. Prior to the experiment, the contrast agent was prepared by combining medical-grade barium sulfate suspension (Micropaque, Guerbet) with low-gelling temperature agarose from Sigma-Aldrich (Ref. A9414). A specific low-gelling temperature agarose was selected for its capacity to maintain a liquid form at room temperature during injection, while also being able to solidify at lower temperatures and remain in a polymerized state when returning to room temperature. The contrast agent was introduced into the bioreactor at 37°C and cooled to around 10°C to trigger polymerization. The resulting hydrogel remained solid until its melting point (approximately 50°C), allowing for X-ray CMT imaging at room temperature. To create the gel solution, 0.2 grams of agarose powder were mixed with 10 milliliters of bacterial culture medium to create a 2% (w/v) concentration. Equal volumes of the barium sulfate suspension and the gel solution were mixed, resulting in a solution of barium sulfate concentration of about 0.5 mg/mL. The barium sulfate suspension was then vacuum filtered using 30 μm nylon filters to eliminate aggregates. The contrast agent was loaded into a sterile syringe and injected at a flow rate 10 times slower than the growth flow rate (0.2 ml/min). After the effluent turned white, indicating that barium sulfate had reached the effluent, the bioreactor was refrigerated at 4°C for 15 minutes to polymerize the gel and prevent sedimentation of the barium sulfate particles.

X-ray image processing Two data sets of images were obtained for each experiment, 1) one prior to biofilm inoculation (DS1), when the porous medium was completely empty and 2) one at the end of a typical experiment where biofilm was left to grow for 4 days (DS2). Histograms are presented in fig. S8. The raw datasets were post-processed using a combination of Amira-Avizo (v2022, ThermoFisher) and IPSDK (v3.2, Reactiv'IP) software. Firstly, the image stack DS2 was translated and rotated in X, Y and Z directions so that it is aligned with the DS1. A non-local means filter was applied to the DS2 dataset and image segmentation was performed on both datasets using a human-trained machine learning algorithm implemented by IPSDK (63). By binarizing the DS1 dataset, the porous material was obtained, while by segmenting the DS2 dataset, the biofilm phase was differentiated from the liquid/micromodel material phase. By subtracting the binarized datasets, three distinct phases were identified: biofilm, liquid phase and solid material phase.

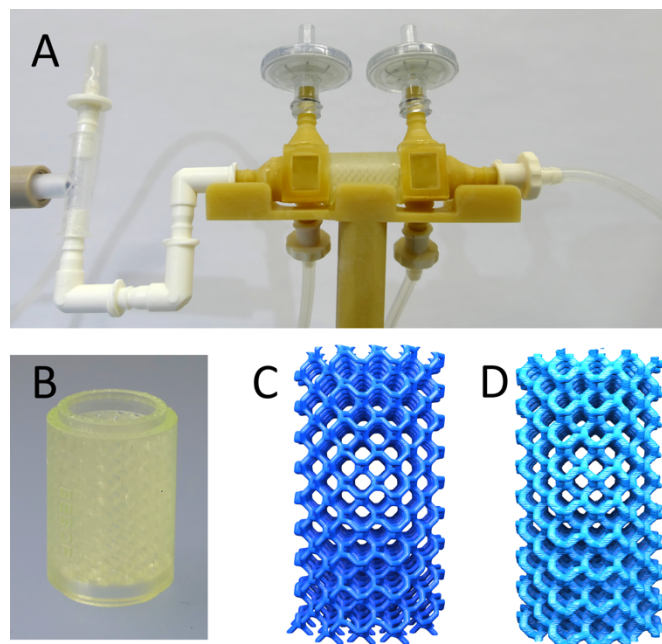


Figure 4 Porous micromodel. (A) Photograph of the micromodel connected to the fluidic system. (B) Central part of the micromodel with the 3D printed (SLA) porous substrate for biofilm growth. The 3D printed part measures 16 mm from top to bottom. (C) 3D visualization of the .stl file initially used for printing. The channel diameters were designed to be 300 μm . (D) X-ray microtomography 3D reconstruction of the printed sample. The resulting diameters were estimated at $315 \pm 18 \mu\text{m}$.

CFD simulations We simulated the flow through the network by solving the incompressible Navier-Stokes equations with no-slip & no-penetration conditions for liquid/solid and liquid/biofilm interfaces. Flow resulted from imposing the velocity at the inlet and a pressure at the outlet. Space discretization was based on the Marker-and-Cell scheme (64) with the unknown velocities evaluated on the faces of mesh elements and the pressure unknowns at the center of each element. The whole 3D domain, including the solid, was discretized using a uniform grid with a local refinement of level 2 near the fluid-solid interface. Non-conforming local refinement was obtained (65) by cutting each edge into 2 equal parts and thus each face and cube into 4 parts. No-slip & no-penetration conditions were approximated by adding a penalization term in the momentum transport equation (66), a standard approach to computing flows with obstacles (67,68). Penalization was 0 in the liquid, so as to recover the Navier-Stokes equations, and -10^{10} times the velocity inside the solid to obtain negligible flow. Error estimations and numerical efficiency were previously established (69). Time discretization was based on a fractional-step of pressure-correction (70). The solver was implemented in the CALIF3S platform (71) developed at the French Institut de Radioprotection et de Sûreté Nucléaire (IRSN). Parallel computations were executed on the CALMIP supercomputer Olympe, based on a domain decomposition approach with METIS (4.0.3) graph partitioner and the OpenMPI (3.1.5) library. At each iteration, the linear system arising from the prediction step was solved using the Generalized Minimal Residual Method. The projection step was solved using the classical conjugate gradient method with an initial stop criterion at 10^{-6} . Stationary state is attained after approximately 300 iterations. The mesh had approximately 25 million mesh cells and required one hour of computation on 288 processors.

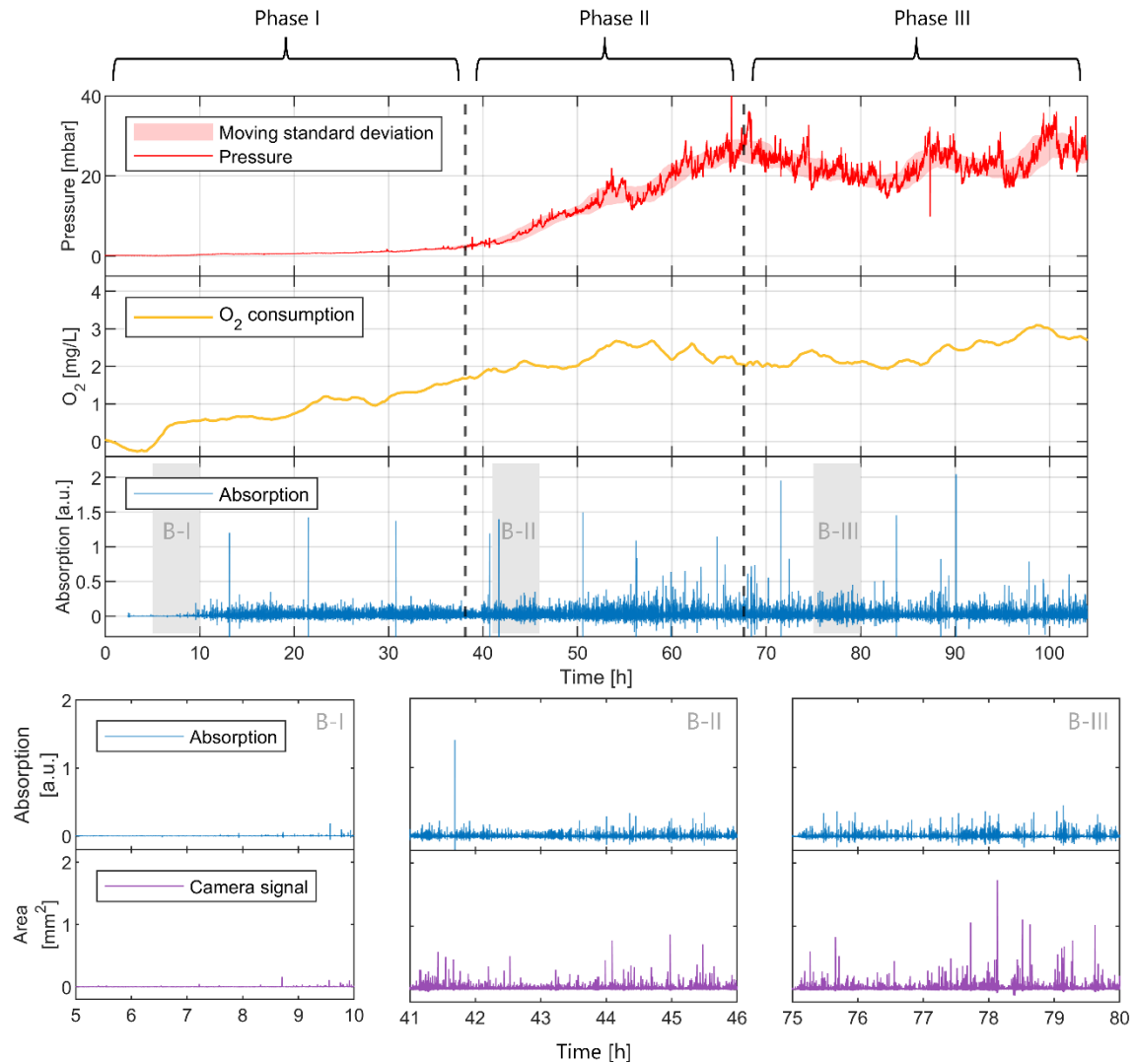


Figure 5 Biofilm development experiment – control experiment is shown in fig. S7. Pressure/oxygen/spectrophotometric/camera measurements of a typical biofilm growth experiment performed using the setup presented in fig. 1A. The biofilm growth experiment was separated in three distinct phases in respect to the evolution of the differential pressure. The pressure moving standard deviation was calculated over 10h of data. For each one of the biofilm growth phases, short videos were taken with the camera module (B-I, B-II and B-III) and were compared to the continuous spectrophotometric data. Initially, no peaks are observed in both camera and spectrophotometric signal indicating that no biofilm detachment is taking place. As the experiment progresses, peak frequency increases. The camera signal is correlated to the area in the video occupied by passing-by biofilm patches giving an indication about their size.

RESULTS AND DISCUSSION

We used X-ray computed microtomography to characterize the four different porous media designs after microfabrication. The aligned bead packing was made of beads of 1mm in diameter and a theoretical porosity, based on a body centered cubic packing arrangement, of 31.98%. The 3D printed fabrication using SLA resulted in a porosity of about 36%, as measured after processing X-ray tomography images. A few pore throats were clogged with the resin as the structure contains overhanging regions that inevitably produce errors due to the lack of a support material in SLA. For comparison, the random bead packing structure with an initial porosity of 37.45% had an actual porosity of about 30% when printed with MJP. X-ray tomography analysis further revealed that some of the pores were clogged with the support material that could not be

removed. The third porous structure was a periodic channel network modelled after a Laves graph. The theoretical porosity was calculated to be 8.56% and the 3D printed version using SLA resulted in a porosity of about 10.6% and channel diameter around 315 μm (see fig. 4 B, C and D). The last porous structure was the random channel network with a theoretical porosity of 9.79%, measured at about 11% after printing and an approximate channel diameter of 250 μm .

Both SLA and MJP can be used to print the porous structure, with respective advantages and disadvantages. The most important difference is the use of a support material for MJP, which eliminates problems associated with overhanging parts, but makes it difficult to thoroughly extract the support material from the porous medium after printing. MJP therefore resulted in lower permeabilities compared to the initial design. We obtained slightly higher porosities and larger channel diameters with SLA, but with a level of

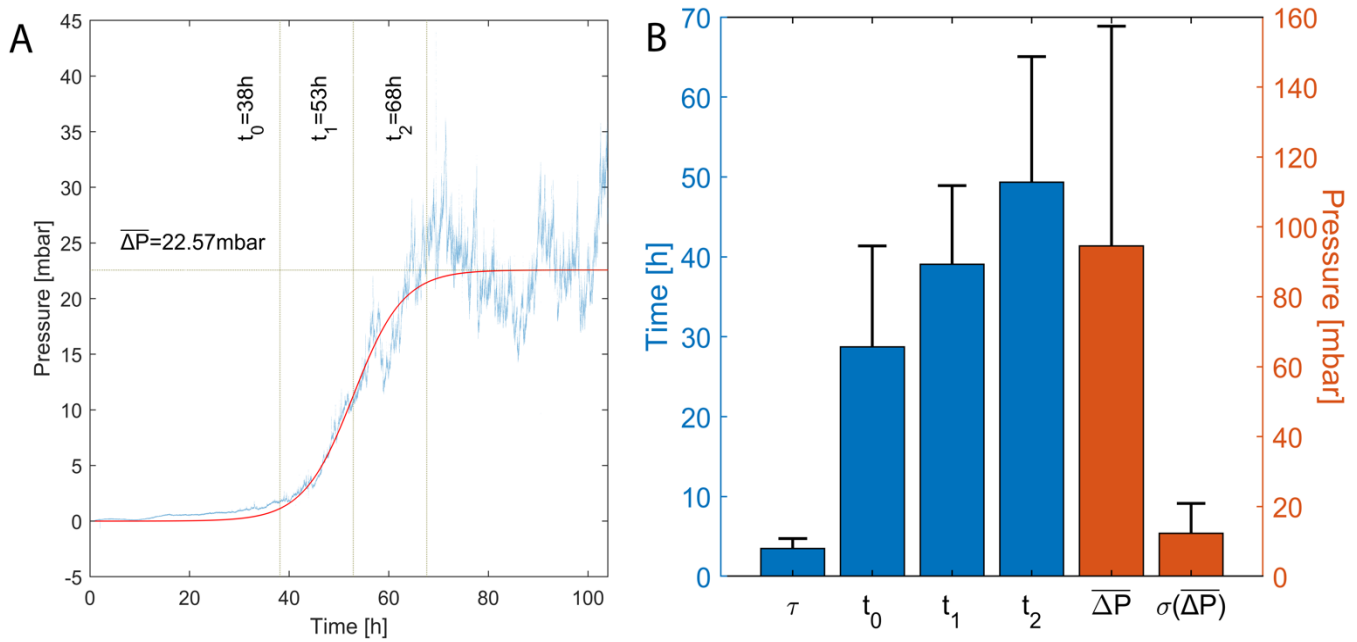


Figure 6 Estimation of the growth parameters based on a logistic fit. (A) Example of logistic fit. (B) Average values of the parameters for 7 independent experiments. $\overline{\Delta P}$ is the average differential pressure at phase III of biofilm growth, t_1 is the value of the function's midpoint, τ is the logistic growth characteristic time of the curve, t_0 the time when biofilm growth transitions from phase I to phase II and t_2 the transitioning time from phase II to phase III. Finally, the standard deviation of the phase III differential pressure fluctuations is noted as $\sigma(\overline{\Delta P})$.

correspondence between the design and the printed structure that was sufficient for our purposes. Our primary goal here was to show the feasibility of fabricating our micromodels with pores in the microfluidic range, using accessible techniques. A more accurate correspondence may be obtained by optimizing e.g. printing parameters, equipment and cleaning procedures after printing for MJF. Physicochemical properties of the interface may also be tailored, for instance through functionalization (72). One fundamental aspect in our case was consistency between printings, even with slight differences compared to the stl design. In that regard SLA provided excellent results, which is compatible with previous studies (73). For the periodic channel network that will be used in the remainder of this work, we estimated a standard deviation of 18 micrometers of the diameter of the channels. The estimation was obtained by measuring the diameter of several channels from three μCT datasets of the same empty porous medium printed in different batches. The measurement was performed on the binarized image stacks.

The network orientation included two types of channels: channels perpendicular to the main direction of flow and channels that have an angle of 45° relative to the main flow direction. The former was named *ChA* and the latter *ChB* to better distinguish between each other (see supplementary information fig. S6). The porous medium has 39 channels B directly connected to the inlet compartment of the micromodel. For the flowrate of 2 ml/min used in the experiments, we calculated that the mean fluid velocity in each of these channels is about $12.1 \text{ mm}\cdot\text{s}^{-1}$ while the Reynolds number is close to 4. The initial permeability of the porous medium was experimentally found equal to $5.26\cdot 10^{-11} \text{ m}^2$ (see supplementary information fig. S1). Further information related to hydrodynamics was extracted from computational fluid dynamics (CFD) simulations of an empty porous medium (see supplementary information fig. S5). The flow in this structure, as shown in supplementary information (fig. S6), features

helicoidal flow paths and channels with zero flow. Type *ChB* channels act as preferential flow paths, while type *ChA* channels exhibit significantly lower velocities compared to *ChB*.

We will now consider biofilm in growth experiments using the setup presented in fig. 1 and fig. 4 with the periodic channel network, showing how it can be used to study biofilm dynamics as well as to monitor biofilm detachment events. The setup includes the water tank module with its UVC bactericidal lamps that is continuously supplying deionised water to the micromodel using a micro-annular gear pump. A second gear pump delivers the necessary nutrients from a sterilized glass bottle to the micromodel. The 3D-printed micromodel's inlet compartment accommodates the water/nutrient injection, a bubble trap module, one end tube of the differential pressure sensor and the UVC quartz window. The outlet compartment accommodates a bubble trap module, the other end tube connected to the differential pressure sensor and the effluent stream and another UVC quartz window. The system is also equipped with sensors that monitor the dissolved oxygen concentration at the water inlet and at the outlet. Finally, the camera and spectrophotometric cells are installed at the effluent stream to directly measure biofilm detachment. A third gear pump is constantly supplying a detergent solution at the outlet of the micromodel to protect the oxygen sensor, the spectrophotometric and the camera cells from biofouling due to their positions in the circuit.

On day 0, the micromodel was inoculated with the bacterial culture according to the protocol described in materials and methods. Figure 5 shows the differential pressure and oxygen measurements, as well as the absorption and camera data. We observed three distinct phases in the evolution of the

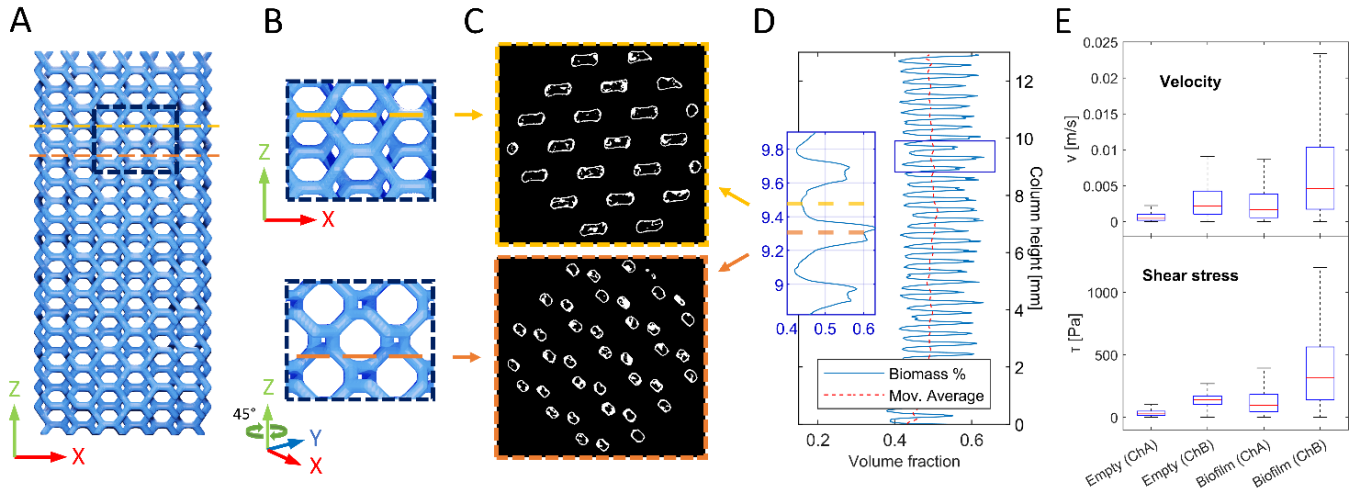


Figure 7 X-ray imaging of biofilm distribution in porous media. (A) Structure of the pore space of the porous medium used for the experiments. The black dashed line box indicates a detailed region in (B). Next, (B) shows a front view (top) and a rotation of 45° around the Z axis (bottom). The dotted yellow and orange lines represent the positions of slices shown in (C). Those slices are binarized images where the white pixels correspond to biofilm. The top image shows a plane populated mainly by type A channels (channels perpendicular to the main flow direction) while the bottom image shows the cross-section of type B channels (channels at 45° from the main flow direction). (D) Slice-by-slice biofilm volume fraction distribution along the length of the porous medium (Z direction). The blue box indicates the region corresponding to the inset. (E) Different channel types exhibit different hydrodynamic environments as demonstrated by the CFD results on an empty and a biofilm inoculated bioreactor. Type A channels appear to experience smaller fluid velocities and shear stresses than type B channels. In addition, biofilm widens the distribution of velocities and shear stresses.

differential pressure, which we quantified by fitting a logistic growth curve to the data (see Figure 6 and material and methods, an approach previously used e.g. in (74)). Phase 1 (from 0 to about $t_0 = 38$ h) is a lag phase where bacteria attached to the porous substrate during the incubation start growing and increase oxygen consumption, but without significantly affecting the hydrodynamics and thus the effective permeability of the porous medium. Absorption data show a progressive increase in the amplitude and frequency of fluctuations, suggesting a range of detachment events as bacteria develop. In the second phase, which ranges from about $t_0 = 38$ h to $t_2 = 68$ h, the biomass is sufficient to induce a steep increase in the pressure difference ($\tau = 5$ h with τ the characteristic time in the logistic growth) across the porous medium. Oxygen consumption peaks and then stabilizes, while fluctuations in absorption due to biofilm detachment keep increasing further compared to phase 1. The third phase, starting at approximately $t_2 = 68$ h, corresponds to a form of permanent regime where the differential pressure oscillates around a plateau ($\overline{\Delta P} \approx 23$ mbar). The global behavior was similar for $n = 7$ independent experiments where biofilm was grown under identical conditions. As shown in fig. 6, logistic fitting applied to pressure data resulted in mean values of $t_0 = 28.75 \pm 9.13$ h, $t_2 = 49.35 \pm 14.53$ h. We also measured a standard deviation of the differential pressure fluctuations of about 25 mbars. Biofilm development in porous media flow thus never seems to reach a steady-state.

Clogging induced by biofilm growth in porous media can lead to large changes in the pressure drop and the permeability. Our results are consistent with this idea, with pressure drop that varied from several mbars in the empty structure to tens of mbars in the porous media colonized by biofilms. High-frequency pressure fluctuations due to the presence of bacteria, such as those evidenced in phases II and III, have been

more rarely observed. It was previously observed that *Leuconostoc mesenteroides* biofilms (29) can generate such fluctuations, with a mechanism based on plugging and plug-propagation through the porous structure. This effect is closely related to the production of dextran and its mechanical properties. *P. aeruginosa* cannot produce dextran and pressure fluctuations in our case are much smaller in amplitude, so that the mechanism inducing these fluctuations is likely different. Recent microfluidic experiments (75) have shown that a competition between growth and shear-induced detachment can generate pressure fluctuations in the same amplitude range for *Bacillus subtilis* biofilms. Opening of flow paths is driven by shear stress causing rupture, while closing results from an increase in the volume of the biomass due to growth. Because pressure fluctuations in our case are also associated with peaks in the spectrophotometric and camera cells, we hypothesize that our observations result from a similar mechanism where the porous medium is saturated in biomass with a stable oxygen consumption but with constant production and flow-induced detachment of biofilm. The fact that this happens for different bacteria and that our structure is 3D with a topology different from that of microfluidic experiments shows that this phenomenon is not specific to 2D systems and may be ubiquitous in applications.

Since fluctuations in the camera and spectrophotometric cells signals are both associated with detachment of biofilm from the micromodel, we therefore expected a form of correlation between both signals. To study further this correspondence, we identified the peaks given by both cells and performed a cross-correlation analysis (fig. S3). Results revealed a strong correlation for a time shift of about 86 seconds between the two signals. This time shift corresponds to the transport of biofilm patches from one cell to the other as the outlet of the micromodel was first connected to the camera cell and then,

after a 30 cm tubing distance, to the spectrophotometric cell. Fourier frequency analysis was performed on the camera and spectrophotometric data for the third phase of biofilm growth, from time 68 to 86 hours to get an insight on the biofilm detachment frequency (see supplementary information). This showed predominant wave components with periods ranging from 4 to 13 minutes for the camera data and 7 to 23 minutes for the camera cell. Data obtained through the camera module further showed the distribution of biofilm patch area with a predominant area of 0.0138 mm² and a mean patch area of 0.0508 mm² (fig. S2).

We further imaged the biofilm spatial distribution within the porous medium using X-ray computed microtomography (fig. 7). Our main objective was to show how our micromodel technology can be combined with 3D imaging and numerical simulations to provide important information about the distribution of the biomass within the porous structure. Biofilm was cultivated in the porous medium according to the same protocol used for monitoring biofilm growth dynamics. After 4 days of growth, the micromodel was stained with the BaSO₄ contrast agent, imaged and the acquired datasets were treated according to the protocol described in materials and methods. The suspension of BaSO₄ particles replaces the liquid phase but particles are large enough to be excluded from the biofilm. This increases the X-ray absorption of the pore space that does not contain biofilm and thus provides a form of “negative contrast” (see details in (61,62)). The volume fraction of the biofilm (slice-by-slice) in the Z-direction in fig. 7D shows that the distribution is overall uniform in the Z direction – the moving average being approximately constant with high-frequency fluctuations related to geometrical features, as detailed in figs. 7A, B and C. However, *ChA* and *B* are colonized differently, with *ChB* containing more biomass than *ChA*. The volume fraction of biofilm was measured to be about 55% in *ChB* and only 42% in *ChA*.

The fact that biofilms do not create uniform films but rather heterogeneous structures in porous media is consistent with a broad range of studies (75,76). This heterogeneity stems from the fact that biofilm development results from complex coupling mechanisms between flow, transport phenomena, bacterial behavior and biofilm growth. Biofilm development can, for instance, lead to fouling and to the formation of both preferential flow pathways (76,77) with large flows and areas that are deprived of nutrients. Biofilm can also induce modifications of flow and transport properties, such as anomalous dispersion. These modifications can then feedback upon the development of biofilms, for example by modifying shear stress and detachment patterns, with different organisms expected to respond differently. Due to these couplings, it has proven difficult to understand what drives biofilm development in porous media flows and to derive general principles. For instance, results in Vandevivere & Baveye (79) suggest that biofilms may develop preferentially in low shear regions, which is not the case in our experiments.

Since the materials used for 3D printing are not completely transparent and have an optical index that does not match that of the culture medium, standard optical microscopy is not easily amenable to imaging of bacterial biofilms in our porous

structures. A variety of techniques have been developed for visualizing biofilms and their impact on flow in porous media, including magnetic resonance (77,78) and X-ray computed microtomography (62,76,80–84). Here, since we have previously validated the approach for *Pseudomonas aeruginosa* in similar conditions (61), we have chosen to use X-ray tomography combined with barium sulfate as a contrast agent. However, if nonspecific sorption to the printed material is sufficiently low, contrast agents such iron sulfate (85) could also be used. Direct tagging of the biofilm, rather than the negative form of contrast obtained with barium sulfate, may open the way towards time-resolved imaging of the dynamics of the colonization. Magnetic resonance could further provide complementary information on flow characteristics that would be extremely valuable in conjunction with simulations.

To explore further the heterogeneity of biomass development and its impact on the flow properties, we computed the solution of incompressible Navier-Stokes equations in the empty porous medium and after biofilm growth, assuming that the biofilm can be treated as a solid phase with a no-penetration/no-slip boundary conditions. Fig. 7E shows results for channels A and B with and without biofilm. In the empty porous medium, we see that the flow is primarily in the vertical channels, as expected. When the porous medium is colonized by biofilms, the average velocity and shear stress increase significantly in both channel types – 258% increase in *ChA* and 110% in *ChB* for the velocity; and 251% increase in *ChA* and 126% in *ChB* for shear. In addition, the distributions of velocity and shear stress is also much larger due to the structure of the biofilm. The biofilm therefore developed preferentially in the vertical channels where the velocities and shear stresses are larger. Growth in the vertical channels induced a stronger change in the value of the average velocity and widened the distribution of velocities and shear stress. Other simulation frameworks could be combined with our technology. Network geometries, such as the one based on Laves graph, may be amenable to modelling using simplified pore-network modelling (86) that consider only connected tubes colonized by biofilms. More detailed modelling approaches (47,87,88) would take into account the growth of the biofilm, its permeability or mechanical properties and deformations. This may even make it possible to measure important properties of biofilms through the resolution of inverse problems combining measured data, imaging and simulations.

Our technology, combined with 3D imaging and CFD, provides a way to explore the dynamics of biofilm development in controlled conditions with embedded instrumentation. Our approach also makes it possible to study virtually any 3D porous structure, opening the path towards a detailed understanding of the role of pore topology and geometry. As discussed in the introduction, this is in contrast with planar microfluidics, including soft lithography, that are limited to quasi-2D flows with anomalous clogging properties and only weak mixing of solutes, such as nutrients. Our platform therefore represents a unique tool to study couplings between biofilm development and transport phenomena in 3D geometries.

CONCLUSIONS

We have developed a novel micromodel technology to explore the dynamics of biofilm development in porous media and experiment new concepts in engineering. Our system implements the following innovations:

- We can fabricate virtually any 3D porous geometry with pores in the range of several hundreds of micrometers to millimeters and a high-level of accuracy and reproducibility and. This approach eliminates issues associated with the variability induced by the porous structure in bead packings classically used for biofilm experiments.
- Unlike standard soft lithography, where pore networks are often constrained into a plane, this approach makes it possible to obtain three-dimensional objects with different topologies and geometries, thus facilitating the study of complex flows and mixing properties beyond quasi-2D systems.
- It is fully instrumented with a differential pressure sensor to estimate clogging; on-line optodes at inlet/outlet to determine oxygen consumption; an on-line spectrophotometer and a camera to measure detachment events.
- UVC is used in the water tank and through quartz windows in the micromodel to limit contaminations and biofouling outside the porous structure. The fluidic system, in particular nutrient and detergent injection, is also designed to minimize such issues.
- The micromodel is in the microfluidic range, thus allowing us to work with small volumes and enabling accurate flows, controlled conditions (e.g. temperature) and high-resolution imaging (X-ray computed microtomography).
- It is based upon modules that can be arranged as needed for specific experiments using standard connectors.
- Most modules are 3D printed, which makes it possible to readily adapt designs and fabricate multiple copies at low cost. It also holds the potential to tune physicochemical properties through functionalization.

Using this system, we have studied the dynamics of *Pseudomonas aeruginosa* development in a periodic network of flow channels. We found that:

- Oxygen consumption reaches a steady-state, but not the pressure drop, which instead features a permanent regime with large temporal fluctuations. These fluctuations reveal a constant detachment and reorganization of the biomass in the porous structure, even after several days. The existence of these fluctuations must be carefully considered in engineering applications, for instance in controlling bioreactors for the production of value-added products or the filtration of pollutants.
- Computational fluid dynamics based on X-ray images suggests that there is a strong heterogeneity in biofilm distribution in

the porous medium and a correlation between flow velocities and biofilm development. Our technological platform is a promising tool to study coupling mechanisms between flow, transport and bacteria in heterogeneous structures.

Conflicts of interest

There are no conflicts to declare.

Acknowledgements

This work is part of a project that has received funding from the European Research Council (ERC) under the European Union's Horizon 2020 research and innovation programme (grant agreement No 803074). It was also partly supported as part of the HoliFAB project funded by the European Union's Horizon 2020 research and innovation program (grant agreement No 760927) and as part of the MultiFAB project funded by FEDER European Regional Funds and French Region Occitanie (grant agreement No 16007407/MP0011594). This work was partially supported by the LAAS-CNRS micro and nanotechnologies platform, a member of the french Renatech network. This work was granted access to the HPC resources of CALMIP supercomputing center under the allocation P23010.

Notes and references

1. Costerton JW, Lewandowski Z, Caldwell DE, Korber DR, Lappin-Scott HM. Microbial Biofilms - Annual Review of Microbiology, 49(1):711. Annu Rev Microbiol. 1995 Jan;49:711–45.
2. Flemming HC, Wuertz S. Bacteria and archaea on Earth and their abundance in biofilms. Nat Rev Microbiol. 2019 Apr;17(4):247–60.
3. Flemming HC, Wingender J, Szewzyk U, Steinberg P, Rice S, Kjelleberg S. Biofilms: An emergent form of bacterial life. Nat Rev Microbiol. 2016 Aug 11;14:563–75.
4. Høiby N, Bjarnsholt T, Givskov M, Molin S, Ciofu O. Antibiotic resistance of bacterial biofilms. Int J Antimicrob Agents. 2010 Apr;35(4):322–32.
5. Høiby N, Ciofu O, Bjarnsholt T. *Pseudomonas aeruginosa* biofilms in cystic fibrosis. Future Microbiol. 2010 Nov;5(11):1663–74.
6. Battin TJ, Besemer K, Bengtsson MM, Romani AM, Packmann AI. The ecology and biogeochemistry of stream biofilms. Nat Rev Microbiol. 2016 Apr;14(4):251–63.

7. Or D, Smets BF, Wraith JM, Dechesne A, Friedman SP. Physical constraints affecting bacterial habitats and activity in unsaturated porous media – a review. *Adv Water Resour.* 2007 Jun 1;30(6):1505–27.
8. Rittmann BE. The significance of biofilms in porous media. *Water Resour Res.* 1993 Jul;29(7):2195–202.
9. Komlos J, Cunningham AB, Camper AK, Sharp RR. Interaction of *Klebsiella oxytoca* and *Burkholderia cepacia* in Dual-Species Batch Cultures and Biofilms as a Function of Growth Rate and Substrate Concentration. *Microb Ecol.* 2005 Jan 1;49(1):114–25.
10. Jonkers HM. Self Healing Concrete: A Biological Approach. In: van der Zwaag S, editor. *Self Healing Materials* [Internet]. Dordrecht: Springer Netherlands; 2007 [cited 2022 Aug 31]. p. 195–204. (Hull R, Jr RMO, Parisi J, Warlimont H, editors. *Springer Series in Materials Science*; vol. 100). Available from: http://link.springer.com/10.1007/978-1-4020-6250-6_9
11. Dhama NK, Reddy MS, Mukherjee A. Biomineralization of Calcium Carbonate Polymorphs by the Bacterial Strains Isolated from Calcareous Sites. *J Microbiol Biotechnol.* 2013;23(5):707–14.
12. Phillips AJ, Lauchnor E, Eldring J (Joe), Esposito R, Mitchell AC, Gerlach R, et al. Potential CO₂ Leakage Reduction through Biofilm-Induced Calcium Carbonate Precipitation. *Environ Sci Technol.* 2013 Jan 2;47(1):142–9.
13. Patel J, Borgohain S, Kumar M, Rangarajan V, Somasundaran P, Sen R. Recent developments in microbial enhanced oil recovery. *Renew Sustain Energy Rev.* 2015 Dec 1;52:1539–58.
14. Boltz JP, Smets BF, Rittmann BE, van Loosdrecht MCM, Morgenroth E, Daigger GT. From biofilm ecology to reactors: a focused review. *Water Sci Technol.* 2017 Apr 28;75(8):1753–60.
15. Nicolella C, van Loosdrecht MCM, Heijnen JJ. Wastewater treatment with particulate biofilm reactors. *J Biotechnol.* 2000 Jun 9;80(1):1–33.
16. Martin I, Wendt D, Heberer M. The role of bioreactors in tissue engineering. *Trends Biotechnol.* 2004 Feb;22(2):80–6.
17. Chen G, Ekama GA, van Loosdrecht MCM, Brdjanovic D, editors. *Biological Wastewater Treatment: Principles, Modeling and Design* [Internet]. 2nd ed. IWA Publishing; 2020 [cited 2022 Nov 8]. Available from: <http://iwaponline.com/ebooks/book/791/Biological-Wastewater-Treatment-Principles>
18. Krishnan MS, Taylor F, Davison BH, Nghiem NP. Economic analysis of fuel ethanol production from corn starch using fluidized-bed bioreactors. *Bioresour Technol.* 2000 Nov 1;75(2):99–105.
19. Cheng KC, Demirci A, Catchmark JM. Advances in biofilm reactors for production of value-added products. *Appl Microbiol Biotechnol.* 2010 Jun 1;87(2):445–56.
20. Vafai K, editor. *Porous Media: Applications in Biological Systems and Biotechnology* [Internet]. 0 ed. CRC Press; 2010 [cited 2022 Sep 2]. Available from: <https://www.taylorfrancis.com/books/9781420065428>
21. Tuson HH, Weibel DB. Bacteria–surface interactions. *Soft Matter.* 2013 Apr 2;9(17):4368–80.
22. Teughels W, Van Assche N, Sliepen I, Quirynen M. Effect of material characteristics and/or surface topography on biofilm development. *Clin Oral Implants Res.* 2006;17(S2):68–81.
23. Krsmanovic M, Biswas D, Ali H, Kumar A, Ghosh R, Dickerson AK. Hydrodynamics and surface properties influence biofilm proliferation. *Adv Colloid Interface Sci.* 2021 Feb 1;288:102336.
24. Formation Criteria for Hyporheic Anoxic Microzones: Assessing Interactions of Hydraulics, Nutrients, and Biofilms - Roy Chowdhury - 2020 - Water Resources Research - Wiley Online Library [Internet]. [cited 2023 Mar 27]. Available from: <https://agupubs.onlinelibrary.wiley.com/doi/10.1029/2019WR025971>

25. Mukherjee S, Bassler BL. Bacterial quorum sensing in complex and dynamically changing environments. *Nat Rev Microbiol.* 2019 Jun;17(6):371–82.
26. Patterns of bacterial motility in microfluidics-confining environments | PNAS [Internet]. [cited 2023 Mar 27]. Available from: <https://www.pnas.org/doi/full/10.1073/pnas.2013925118>
27. de Anna P, Pahlavan AA, Yawata Y, Stocker R, Juanes R. Chemotaxis under flow disorder shapes microbial dispersion in porous media. *Nat Phys.* 2021 Jan;17(1):68–73.
28. Kim MK, Ingremeau F, Zhao A, Bassler BL, Stone HA. Local and global consequences of flow on bacterial quorum sensing. *Nat Microbiol.* 2016 Jan;1(1):15005.
29. Stewart TL, Fogler HS. Biomass plug development and propagation in porous media. *Biotechnol Bioeng.* 2001 Feb 5;72(3):353–63.
30. Perez LJ, Parashar R, Plymale A, Scheibe TD. Contributions of biofilm-induced flow heterogeneities to solute retention and anomalous transport features in porous media. *Water Res.* 2022 Feb 1;209:117896.
31. Drescher K, Shen Y, Bassler BL, Stone HA. Biofilm streamers cause catastrophic disruption of flow with consequences for environmental and medical systems. *Proc Natl Acad Sci.* 2013 Mar 12;110(11):4345–50.
32. Karimi A, Karig D, Kumar A, Ardekani AM. Interplay of physical mechanisms and biofilm processes: review of microfluidic methods. *Lab Chip.* 2014 Dec 3;15(1):23–42.
33. Yawata Y, Nguyen J, Stocker R, Rusconi R. Microfluidic Studies of Biofilm Formation in Dynamic Environments. *J Bacteriol.* 198(19):2589–95.
34. Rusconi R, Garren M, Stocker R. Microfluidics Expanding the Frontiers of Microbial Ecology. *Annu Rev Biophys.* 2014;43(1):65–91.
35. Duncombe TA, Tentori AM, Herr AE. Microfluidics: reframing biological enquiry. *Nat Rev Mol Cell Biol.* 2015 Sep;16(9):554–67.
36. Marques MP, Szita N. Bioprocess microfluidics: applying microfluidic devices for bioprocessing. *Curr Opin Chem Eng.* 2017 Nov 1;18:61–8.
37. Pasirayi G, Auger V, Scott SM, Rahman PKSM, Islam M, O`Hare L, et al. Microfluidic Bioreactors for Cell Culturing: A Review. *Micro Nanosyst.* 3(2):137–60.
38. Bjork SM, Joensson HN. Microfluidics for cell factory and bioprocess development. *Curr Opin Biotechnol.* 2019 Feb 1;55:95–102.
39. Perez-Pinera P, Han N, Cleto S, Cao J, Purcell O, Shah KA, et al. Synthetic biology and microbioreactor platforms for programmable production of biologics at the point-of-care. *Nat Commun.* 2016 Jul 29;7(1):12211.
40. Hegab HM, ElMekawy A, Stakenborg T. Review of microfluidic microbioreactor technology for high-throughput submerged microbiological cultivation. *Biomicrofluidics.* 2013 Apr 5;7(2):021502.
41. Schäpper D, Alam MNHZ, Szita N, Eliasson Lantz A, Gernaey KV. Application of microbioreactors in fermentation process development: a review. *Anal Bioanal Chem.* 2009 Oct;395(3):679–95.
42. Qin N, Zhao P, Ho EA, Xin G, Ren CL. Microfluidic Technology for Antibacterial Resistance Study and Antibiotic Susceptibility Testing: Review and Perspective. *ACS Sens.* 2021 Jan 22;6(1):3–21.
43. Hoffmann M, Schlüter M, Rübiger N. Experimental investigation of liquid–liquid mixing in T-shaped micro-mixers using μ -LIF and μ -PIV. *Chem Eng Sci.* 2006 May 1;61(9):2968–76.
44. Beaudoin A, de Dreuzy JR. Numerical assessment of 3-D macrodispersion in heterogeneous porous media. *Water Resour Res.* 2013;49(5):2489–96.
45. Shimizu R, Tanaka H. Impact of complex topology of porous media on phase separation of binary mixtures. *Sci Adv.* 2017 Dec 22;3(12):eaap9570.
46. Bernabé Y, Li M, Mainault A. Permeability and pore connectivity: A new model based on network

- simulations. *J Geophys Res Solid Earth* [Internet]. 2010 [cited 2023 Apr 4];115(B10). Available from: <https://onlinelibrary.wiley.com/doi/abs/10.1029/2010JB007444>
47. von der Schulenburg DAG, Pintelon TRR, Picioreanu C, Van Loosdrecht MCM, Johns ML. Three-dimensional simulations of biofilm growth in porous media. *AIChE J*. 2009;55(2):494–504.
 48. Stoodley P, Cargo R, Rupp CJ, Wilson S, Klapper I. Biofilm material properties as related to shear-induced deformation and detachment phenomena. *J Ind Microbiol Biotechnol*. 2002 Dec 1;29(6):361–7.
 49. Groisman A, Steinberg V. Efficient mixing at low Reynolds numbers using polymer additives. *Nature*. 2001 Apr;410(6831):905–8.
 50. Ottino JM, Wiggins SR, Wiggins S, Ottino JM. Foundations of chaotic mixing. *Philos Trans R Soc Lond Ser Math Phys Eng Sci*. 2004 May 15;362(1818):937–70.
 51. Stroock AD, Dertinger SKW, Ajdari A, Mezic I, Stone HA, Whitesides GM. Chaotic mixer for microchannels. *Science*. 2002 Jan 25;295(5555):647–51.
 52. Heyman J, Lester DR, Le Borgne T. Scalar Signatures of Chaotic Mixing in Porous Media. *Phys Rev Lett*. 2021 Jan 22;126(3):034505.
 53. Turuban R, Lester DR, Heyman J, Borgne TL, Méheust Y. Chaotic mixing in crystalline granular media. *J Fluid Mech*. 2019 Jul;871:562–94.
 54. Lester DR, Dentz M, Borgne TL. Chaotic mixing in three-dimensional porous media. *J Fluid Mech*. 2016 Sep;803:144–74.
 55. Jang H, Rusconi R, Stocker R. Biofilm disruption by an air bubble reveals heterogeneous age-dependent detachment patterns dictated by initial extracellular matrix distribution. *Npj Biofilms Microbiomes*. 2017 Mar 3;3(1):1–7.
 56. Foundation B. blender.org - Home of the Blender project - Free and Open 3D Creation Software [Internet]. blender.org. [cited 2023 Feb 25]. Available from: <https://www.blender.org/>
 57. Smith AF, Doyeux V, Berg M, Peyrounette M, Haft-Javaherian M, Larue AE, et al. Brain Capillary Networks Across Species: A few Simple Organizational Requirements Are Sufficient to Reproduce Both Structure and Function. *Front Physiol* [Internet]. 2019 [cited 2019 Sep 17];10. Available from: <https://www.frontiersin.org/articles/10.3389/fphys.2019.00233/full>
 58. Coxeter HSM. On Laves' Graph Of Girth Ten. *Can J Math*. 1955 ed;7:18–23.
 59. Torkzadeh H, Cates EL. Biofilm growth under continuous UVC irradiation: Quantitative effects of growth conditions and growth time on intensity response parameters. *Water Res*. 2021 Nov;206:117747.
 60. Ramos G, Toulouze C, Rima M, Liot O, Duru P, Davit Y. Ultraviolet control of bacterial biofilms in microfluidic chips. *Biomicrofluidics*. 2023 Mar 1;17(2):024107.
 61. Larue AE, Swider P, Duru P, Daviaud D, Quintard M, Davit Y. Quantitative 3D comparison of biofilm imaged by X-ray micro-tomography and two-photon laser scanning microscopy: QUANTITATIVE 3D COMPARISON OF BIOFILM. *J Microsc*. 2018 Sep;271(3):302–14.
 62. Davit Y, Iltis G, Debenest G, Veran-Tissoires S, Wildenschild D, Gerino M, et al. Imaging biofilm in porous media using X-ray computed microtomography. *J Microsc*. 2011;242(1):15–25.
 63. Reactiv IP [Internet]. [cited 2023 Mar 28]. Reactiv'IP - Smart Image Processing. Available from: <https://www.reactivip.com/>
 64. Patankar SV. Numerical Heat Transfer and Fluid Flow [Internet]. 1st ed. CRC Press; 2018 [cited 2023 Mar 9]. Available from: <https://www.taylorfrancis.com/books/9781482234213>
 65. Chénier E, Eymard R, Gallouët T, Herbin R. An extension of the MAC scheme to locally refined meshes: convergence analysis for the full tensor time-dependent Navier–Stokes equations. *Calcolo*. 2015 Mar;52(1):69–107.

66. Khadra K, Angot P, Parneix S, Caltagirone JP. Fictitious domain approach for numerical modelling of Navier-Stokes equations. *Int J Numer Methods Fluids*. 2000 Dec 30;34(8):651–84.
67. Bruneau CH, Fabrie P. Effective downstream boundary conditions for incompressible Navier–Stokes equations. *Int J Numer Methods Fluids*. 1994;19(8):693–705.
68. Boiron O, Chiavassa G, Donat R. A high-resolution penalization method for large Mach number flows in the presence of obstacles. *Comput Fluids*. 2009 Mar 1;38(3):703–14.
69. Angot P, Bruneau CH, Fabrie P. A penalization method to take into account obstacles in incompressible viscous flows. *Numer Math*. 1999 Feb 1;81(4):497–520.
70. Guermond JL, Mineev P, Shen J. An overview of projection methods for incompressible flows. *Comput Methods Appl Mech Eng*. 2006 Sep;195(44–47):6011–45.
71. Project Home - CALIF3S - MyGForge [Internet]. [cited 2023 Apr 4]. Available from: <https://gforge.irsn.fr/#/project/calif3s>
72. Su CK. Review of 3D-Printed functionalized devices for chemical and biochemical analysis. *Anal Chim Acta*. 2021 May 8;1158:338348.
73. Bodaghi M, Ban D, Mobin M, Park CH, Lomov SV, Nikzad M. Additively manufactured three dimensional reference porous media for the calibration of permeability measurement set-ups. *Compos Part Appl Sci Manuf*. 2020 Dec 1;139:106119.
74. Scheidweiler D, Peter H, Pramateftaki P, de Anna P, Battin TJ. Unraveling the biophysical underpinnings to the success of multispecies biofilms in porous environments. *ISME J*. 2019 Jul;13(7):1700–10.
75. Kurz DL, Secchi E, Carrillo FJ, Bourg IC, Stocker R, Jimenez-Martinez J. Competition between growth and shear stress drives intermittency in preferential flow paths in porous medium biofilms. *Proc Natl Acad Sci*. 2022 Jul 26;119(30):e2122202119.
76. Carrel M, Morales VL, Beltran MA, Derlon N, Kaufmann R, Morgenroth E, et al. Biofilms in 3D porous media: Delineating the influence of the pore network geometry, flow and mass transfer on biofilm development. *Water Res*. 2018 May 1;134:280–91.
77. Herrling MP, Lackner S, Nirschl H, Horn H, Guthausen G. Recent NMR/MRI studies of biofilm structures and dynamics. In: *Annual Reports on NMR Spectroscopy*. Academic Press Inc.; 2019. p. 163–213.
78. Seymour JD, Gage JP, Codd SL, Gerlach R. Anomalous fluid transport in porous media induced by biofilm growth. *Phys Rev Lett*. 2004 Nov;93(19):198103.
79. Vandevivere P, Baveye P. Effect of bacterial extracellular polymers on the saturated hydraulic conductivity of sand columns. *Appl Environ Microbiol*. 1992 May;58(5):1690–8.
80. Iltis GC, Armstrong RT, Jansik DP, Wood BD, Wildenschild D. Imaging biofilm architecture within porous media using synchrotron-based X-ray computed microtomography. *Water Resour Res* [Internet]. 2011 Feb;47(2).
81. Ostvar S, Iltis G, Davit Y, Schlüter S, Andersson L, Wood BD, et al. Investigating the influence of flow rate on biofilm growth in three dimensions using microimaging. *Adv Water Resour*. 2018 Jul;117:1–13.
82. Wildenschild D, Rivers ML, Porter ML, Iltis GC, Armstrong RT, Davit Y, et al. Using Synchrotron-Based X-Ray Microtomography and Functional Contrast Agents in Environmental Applications. In 2013.
83. Rolland du Roscoat S, Martins JMF, Séchet P, Vince E, Latil P, Geindreau C. Application of synchrotron X-ray microtomography for visualizing bacterial biofilms 3D microstructure in porous media. *Biotechnol Bioeng*. 2014 Jun;111(6):1265–71.
84. Rolland du Roscoat S, Ivankovic T, Lenoir N, Dekic S, Martins JMF, Geindreau C. First visualisation of bacterial biofilms in 3D porous media with neutron microtomography without contrast agent. *J Microsc*. 2022;285(1):20–8.

85. Carrel M, Beltran MA, Morales VL, Derlon N, Morgenroth E, Kaufmann R, et al. Biofilm imaging in porous media by laboratory X-Ray tomography: Combining a non-destructive contrast agent with propagation-based phase-contrast imaging tools. *PLoS ONE*. 2017 Jul;12(7):e0180374.
86. Thullner M, Baveye P. Computational pore network modeling of the influence of biofilm permeability on bioclogging in porous media. *Biotechnol Bioeng*. 2008 Apr 15;99(6):1337–51.
87. Sudarsan R, Ghosh S, Stockie JM, Eberl HJ. Simulating Biofilm Deformation and Detachment with the Immersed Boundary Method. *Commun Comput Phys*. 2016 Mar;19(3):682–732.
88. Peszynska M, Trykozko A, Iltis G, Schlueter S, Wildenschild D. Biofilm growth in porous media: Experiments, computational modeling at the porescale, and upscaling. *Adv Water Resour*. 2016 Sep;95:288–301.